

X-ray phase-contrast imaging at 100 keV

T. Thüring, M. Abis, and M. Stampanoni

Paul Scherrer Institut, Villigen PSI, Switzerland and

Institute for Biomedical Engineering,

Swiss Federal Institute of Technology, Zurich, Switzerland

Z. Wang and C. David

Paul Scherrer Institut, Villigen PSI, Switzerland

(Dated: September 3, 2013)

Abstract

Phase contrast imaging with X-rays provides access to complementary physical contrast mechanisms. Phase sensitive imaging in the diagnostic energy range between 80 and 150 keV is still largely unexplored, as the current methods typically entail severe technical challenges. A phase-contrast technique at such high energies is of scientific and industrial interest as it vastly expands the range of applications, for instance, by the examination of materials of high density or thickness. The approach includes a new design for the grating manufacturing in Talbot-Lau interferometry, with an edge-on illumination and curved structures to match the beam divergence. The edge-on approach breaks the current limits of achievable grating aspect ratios, which has been a key issue for a long time. The curvature of the gratings solves the intrinsic reduction of the field of view which occurs for gratings with such high aspect ratios and allows for a very compact setup, with a distance of 31 cm between the source grating and the analyzer grating. Using an imaging arrangement based on a conventional X-ray tube, phase and dark-field contrast imaging at 100 keV is demonstrated. This achievement paves the road for the transfer of phase-contrast imaging into fields where high energies are required, such as medical computed tomography, chip failure analysis or homeland security.

X-ray radiography and computed tomography (CT) are nowadays standard imaging techniques in materials and life sciences for the nondestructive examination of samples or the diagnosis of diseases in patients. The underlying contrast mechanism relies on the different X-ray attenuation properties of different materials or tissue types. The dominant physical effects contributing to attenuation are the photoelectric effect and incoherent (Compton) scattering. The sum of their contributions determines the attenuation coefficient, which is a wavelength dependent material parameter. Besides attenuation, the wave nature of X-rays reveals another contrast mechanism, which is the phase shift. The interaction contributing to phase shifts is coherent (Rayleigh) scattering [1].

Using the material parameter $n = 1 - \delta(\mathbf{r}, \lambda) + i\beta(\mathbf{r}, \lambda)$, known from X-ray wave optics as the complex index of refraction, the wavelength dependent attenuation and phase shift properties of an object at the spatial coordinate \mathbf{r} are fully described. The imaginary part $\beta(\mathbf{r}, \lambda)$ is related to the attenuation per unit length (attenuation coefficient) by $\mu = 4\pi\beta(\mathbf{r}, \lambda)/\lambda$ and the total attenuation by an object of thickness d can be described by the line integral $L_\mu = \int_0^d \mu(\mathbf{r}, \lambda) dl$. Similarly, the real part $\delta(\mathbf{r}, \lambda)$ determines the phase shift per unit length by $\phi = 2\pi\delta/\lambda$ and the total phase shift is $L_\phi = \int_0^d \phi(\mathbf{r}) dl$.

While the attenuation line integral L_μ can be directly measured with an X-ray detector by measuring the reduction of the beam intensity I ($L_\mu \propto \log(I)$), the measurement of the phase shift integral L_ϕ is more challenging as there is no such simple relation. However, phase sensitive imaging is a desirable modality, as it can provide an enhanced contrast-to-noise ratio (CNR) in images compared to attenuation for certain materials or in different tissues [2, 3]. Furthermore, the refractive index decrement δ provides direct access to the electron density [1] and in combination with attenuation, it further enables the determination of the effective atomic number of a material [4].

In the past, a lot of effort has been invested into the development of techniques which are sensitive to the phase shift. Since most of the available phase contrast techniques rely on interference and thus typically on optical hardware (e.g. crystals, gratings), they vary a lot in terms of sensitivity, practical applicability or achievable resolution. The vast majority of the methods, including crystal analyzer based [5, 6] or interferometric [7, 8] methods rely on X-ray beams of high spatial and temporal coherence, which is available only at synchrotron sources. Techniques which are compatible with an X-ray beam of low temporal coherence (broad bandwidth) are the in-line phase contrast method [9–11] and Talbot interferometry

[12–14]. Phase-contrast imaging using X-ray beams of low temporal *and* spatial coherence such as conventional low-brilliance X-ray tubes have been demonstrated with Talbot-Lau interferometry [15] and coded apertures [16].

Talbot interferometry has been demonstrated using a synchrotron source at 82 keV [17] and 123 keV[?]. Using a low-brilliance X-ray tube, Talbot-Lau interferometry was applied at 60 keV mean energy [18]. Medical imaging applications may benefit from phase contrast at higher energies: chest or abdominal radiography or CT require energies between 100 and 150 keV. Other potential applications are homeland security or chip failure analysis, which require high energies for the visualization of materials of high density and atomic number.

Here, we introduce a method for phase-contrast imaging which is compatible with the entire diagnostic energy range of X-rays. Moreover, the method is fully compatible with compact imaging arrangements based on conventional X-ray tubes. The method is based on Talbot-Lau interferometry [15] and employs an edge-on approach for the grating design and arrangement. The challenge which limited the progress towards higher energies was mainly related to the manufacturing of gratings with high aspect ratios. The aspect ratio, given by

$$\text{AR} = \frac{2h}{p}, \quad (1)$$

where p is the grating period and h the grating structure height, is normally limited by the lithographic process, as grating structures tend to collapse or to deform (e.g. through capillary forces) if the aspect ratio is too high. For a given setup distance these parameters depend on the target energy E according to $p \propto 1/\sqrt{E}$ and $h \propto E^3$, and therefore $\text{AR} \propto E^{7/2}$ [14]. If at $E = 25$ keV an aspect ratio for the absorption grating of around $\text{AR} = 30$ is necessary for a reasonable length of the experimental arrangement, it would have to be at least 128 for $E = 100$ keV. Moreover, when using a broad spectrum, photons above the design energy should also be efficiently attenuated by the gratings, which requires even higher aspect ratios. Maximum achievable aspect ratios of current grating fabrication techniques [19, 20] are approximately around 60, larger values are often not achievable or come at the expense of a very poor grating quality and performance.

Our design introduces the edge-on illumination of circularly aligned structures. Edge-on illumination (figure 1), as opposed to face-on illumination, exploits the dimension along the grating lines to form a high aspect ratio of the structures in direction of the beam. The effective structure height of the grating is then determined by the grating dimension along

the grating lines, which essentially allows arbitrarily high aspect ratios.

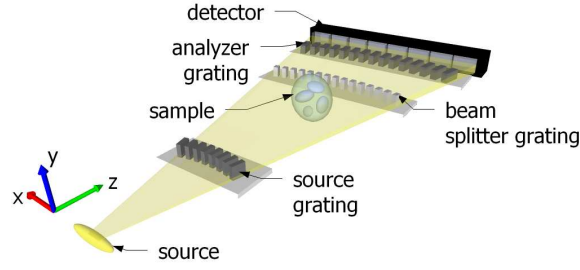


FIG. 1. Schematic of a grating interferometer for X-ray energies between 60 and 150 keV in edge-on illumination mode. The aspect ratio is defined by the ratio of the travelling distance along the grating lines and the period and can be arbitrarily long. In order to avoid a reduction of the field of view, the grating structures are aligned on an arc.

Increasing the aspect ratio of the gratings typically leads to a reduction of the field of view due to the change of the grating transmission function at high incident angles, which has also been identified by using a glancing angle of the gratings between zero and 90° [21]. In order to overcome this problem, the grating lines are circularly aligned with a radius equal to the distance to the source.

The combination of edge-on illumination and circularly aligned structures enables phase-contrast imaging at arbitrary design energies and with a maximum field of view in the horizontal direction (x direction). These advantages come at the expense of a limited field of view in the vertical direction (y direction), which is, depending on the X-ray detector, typically a few pixels. However, radiographic 2D imaging is possible in scanning mode, without increasing dose. Similarly, for tomographic images, the approach allows single slice CT or full 3D imaging in scanning mode.

Grating design and fabrication is nonstandard and involves a complex mask design, as shown in Figure 2. Each grating resides on a silicon chip and has its specific structure length and curvature. For the current experiments, a symmetric interferometer with a grating period of $p = 2.8 \mu\text{m}$ for all gratings has been used. The design energy is 100 keV and the beam splitter grating periodically shifts the phase by zero and π at this energy [13]. Using gold as the phase shifting material, this requires a structure length of $h_1 = 19.8 \mu\text{m}$. The analyzer grating is an absorption mask for sensing slight changes of the interference

pattern generated by the beam splitter [14]. With a structure length of $h_2 = 800\text{ }\mu\text{m}$, this grating has an aspect ratio of $2h/p \approx 570$ and thus sufficiently attenuates X-rays up to energies of 160 keV. Beam splitter- and analyzer grating are separated at the first fractional Talbot order [22], resulting in an intergrating distance of 158 mm. The source grating splits the relatively large focal spot ($\sim 1\text{ mm}$) into an array of individually coherent, but mutually incoherent sources [15]. It is also made of gold structures with a structure length of $h_0 = h_2 = 800\text{ }\mu\text{m}$.

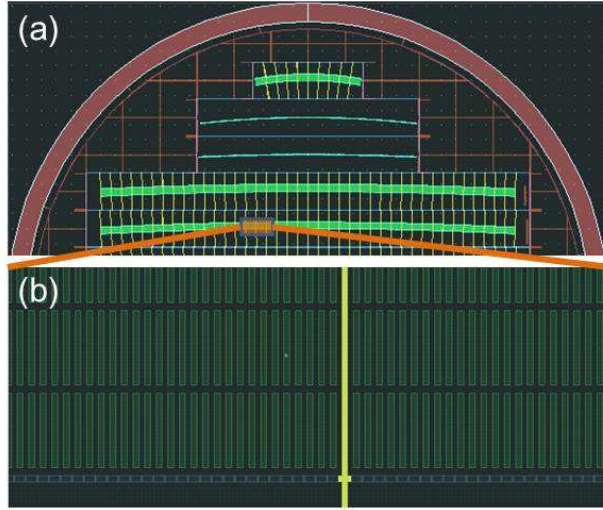


FIG. 2. Grating design mask for the edge-on illumination approach. (a) Top part of the 4 inch wafer, showing five grating chips; one source grating, two beam splitter gratings and two analyzer gratings (from top to bottom). The gratings have different curvatures which are specific to the grating interferometer geometry. (b) Zoom into the grating structures, contain interrupting bridges used for stabilizing the grating structures in the lithographic process [20].

Due to the high spectral acceptance [22, 23] of the interferometer (50 keV to $> 160\text{ keV}$) and the high attenuation efficiencies of the source- and analyzer gratings ($> 90\%$ up to 160 keV), the voltage of the X-ray source was set to the maximum of 160 kV. With a grating structure height of approx. $100\text{ }\mu\text{m}$, the field of view in the vertical direction is limited to one detector pixel row. In the horizontal direction, the field of view is limited by the grating size and the geometric magnification of the sample, yielding a maximum field of view of 30 mm. In addition to the standard components (source, camera, interferometer), two optical slits, one in front of the source grating, the other in front of the camera, were required for the collimation of the beam in the vertical direction. X-rays which are not

travelling through all of the gratings do not contribute to the signal and are attenuated by the slits.

Fig. 3 shows a radiographic scan of an electronic chip. Several resistors and an integrated circuits are located on different layers on the chip. The images were acquired in scanning mode, using a step size of $100\text{ }\mu\text{m}$ along the y axis. For a better comparison of the magnified phase and attenuation images, the attenuation image has been replaced with the differential attenuation image, which was obtained by digital differentiation. In the attenuation image, the contrast of the soldering points of the integrated circuit is reduced underneath the resistors, while in the phase image, they can clearly be identified. This shows the benefit of the phase nature of the image, which may be useful to identify flaws in multilayered structures such as electronic chips.

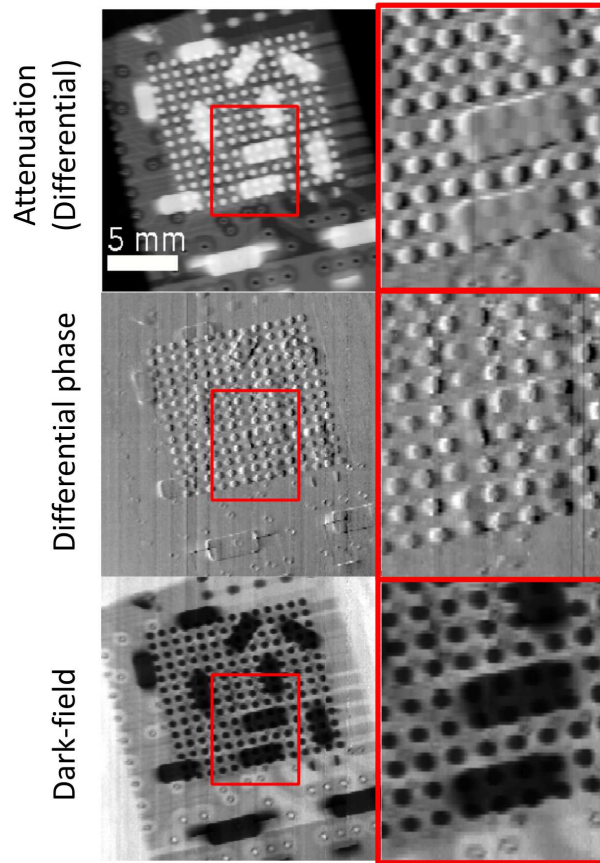


FIG. 3. Radiographic scan of an electronic chip. The image was acquired with 24 phase steps and an exposure time of 15 s per step. The top right image shows the differential absorption image.

Edge-on illuminated grating interferometry breaks the current limitations of phase-

contrast imaging to the lower diagnostic energy range. Compact geometries using conventional X-ray sources for design energies well above 100 keV could be realized with the approach. This enables the examination of materials of higher density or thickness which would be intransparent at lower energies. Finally, the approach is not limited to X-ray imaging, but could easily be applied to other grating-based imaging modalities (e.g., with neutrons [24]) where high aspect ratios are required.

METHODS

Edge-on illuminated gratings were manufactured by Micro Works GmbH, Germany, using a LIGA process [20]. Each grating resides on a $5 \times 60 \text{ mm}^2$ silicon chip and several grating chips are fabricated on a single 4 inch silicon wafer. The experimental arrangement for a design energy at 100 keV is a symmetric Talbot-Lau interferometer with a grating period of $p = 2.8 \mu\text{m}$ for all gratings. The distance from the source grating to the analyzer grating is 32 cm and the source grating is positioned 23 cm away from the source. The number of phase steps for one projection was 24 [22] and the exposure time for the images was 15 seconds per phase step.

The X-ray source is a COMET MXR-160HP/11 X-ray tube with a maximum output voltage of 160 kV. In the experiment, it was set to the maximum voltage. The focal spot size is approximately 1 mm. The detector is a CCD camera from Finger Lakes Instruments. A cesium iodide (CsI:Ti) scintillator of 600 μm thickness converts the X-rays to visible light and is coupled with an optical lens projecting the image onto the CCD. The effective pixel size is 80 μm . The widths of the collimating slits are 25 μm and 100 μm , respectively.

In Fig. 3, image acquisition involved 24 phase steps [22] and an exposure time of 15 seconds per step. The long exposure times are mostly constrained by the low average visibility of the gratings (5 %). As the quality in the manufacturing of the structure increases, the exposure time can become substantially shorter.

ACKNOWLEDGEMENTS

We thank Gordan Mikuljan from Paul Scherrer Institute, Switzerland, for his work on the mechanical design, Joachim Schulz and Marco Walter from Microworks GmbH, Germany,

for the competent support on grating design issues, Christian Kottler and Vincent Revol from Centre Suisse d'Electronique et de Microtechnique (CSEM), Switzerland for the fruitful discussions on the design of the system. Part of this work has been supported by the ERC Grant ERC-2012-StG 310005-PhaseX.

-
- [1] J. Als-Nielsen and D. McMorrow, *Elements of modern X-ray physics* (2011).
 - [2] F. Pfeiffer, O. Bunk, C. David, M. Bech, G. Le Duc, A. Bravin, and P. Cloetens, *Physics in medicine and biology* **52**, 6923 (2007).
 - [3] S. A. McDonald, F. Marone, C. Hintermuller, G. Mikuljan, C. David, F. Pfeiffer, M. Stamparoni, and C. Hintermüller, *Journal of Synchrotron Radiation* **16**, 562 (2009).
 - [4] Z. Qi, J. Zambelli, N. Bevins, and G. Chen, *Physics in medicine and biology* **55**, 2669 (2010).
 - [5] T. Davis, D. Gao, T. Gureyev, A. Stevenson, and S. Wilkins, *Nature* **373**, 595 (1995).
 - [6] D. Chapman, W. Thomlinson, R. Johnston, D. Washburn, E. Pisano, N. Gmür, Z. Zhong, R. Menk, F. Arfelli, and D. Sayers, *Physics in Medicine and Biology* **42**, 2015 (1997).
 - [7] U. Bonse and M. Hart, *Applied Physics Letters* **6**, 155 (1965).
 - [8] A. Momose, T. Takeda, Y. Itai, and K. Hirano, *Nature Medicine* **2**, 473 (1996).
 - [9] A. Snigirev, I. Snigireva, V. Kohn, S. Kuznetsov, and I. Schelokov, *Review of Scientific Instruments* **66**, 5486 (1995).
 - [10] S. Wilkins, T. Gureyev, D. Gao, A. Pogany, and A. Stevenson, *Nature* **384**, 335 (1996).
 - [11] P. Cloetens, R. Barrett, J. Baruchel, J. Guigay, and M. Schlenker, *Journal of Physics D: Applied Physics* **29**, 133 (1996).
 - [12] P. Cloetens, J. Guigay, C. De Martino, J. Baruchel, and M. Schlenker, *Optics letters* **22**, 1059 (1997).
 - [13] C. David, B. Nöhammer, H. Solak, and E. Ziegler, *Applied Physics Letters* **81**, 3287 (2002).
 - [14] A. Momose, S. Kawamoto, I. Koyama, Y. Hamaishi, K. Takai, and Y. Suzuki, *Japanese Journal of Applied Physics* **42**, L866 (2003).
 - [15] F. Pfeiffer, T. Weitkamp, O. Bunk, and C. David, *Nature Physics* **2**, 258 (2006).
 - [16] P. Munro, K. Ignatyev, R. Speller, and A. Olivo, *Proceedings of the National Academy of Sciences* **2012**, 2 (2012).

- [17] M. Willner, M. Bech, J. Herzen, I. Zanette, D. Hahn, J. Kenntner, J. Mohr, A. Rack, T. Weitkamp, and F. Pfeiffer, *Optics express* **21**, 4155 (2013).
- [18] T. Donath, M. Chabior, F. Pfeiffer, O. Bunk, E. Reznikova, J. Mohr, E. Hempel, S. Popescu, M. Hoheisel, M. Schuster, J. Baumann, and C. David, *Journal of Applied Physics* **106**, 054703 (2009).
- [19] C. David, J. Bruder, T. Rohbeck, C. Grünzweig, C. Kottler, A. Diaz, O. Bunk, and F. Pfeiffer, *Microelectronic Engineering* **84**, 1172 (2007).
- [20] J. Kenntner, T. Grund, B. Matthis, M. Boerner, J. Mohr, T. Scherer, M. Walter, M. Willner, A. Tapfer, M. Bech, F. Pfeiffer, I. Zanette, and T. Weitkamp, in *Proceedings of SPIE*, Vol. 7804 (2010) p. 780408.
- [21] D. Stutman and M. Finkenthal, *Applied physics letters* **101**, 91108 (2012).
- [22] T. Weitkamp, A. Diaz, C. David, F. Pfeiffer, M. Stampanoni, P. Cloetens, and E. Ziegler, *Optics Express* **13**, 6296 (2005).
- [23] T. Thuering, W. Barber, Y. Seo, F. Alhassen, J. Iwanczyk, and M. Stampanoni, *Applied Physics Letters* **102**, 191113 (2013).
- [24] C. Grünzweig, F. Pfeiffer, O. Bunk, T. Donath, G. Kühne, G. Frei, M. Dierolf, and C. David, *The Review of scientific instruments* **79**, 053703 (2008).